Core-excited states of SF_6 probed with soft-x-ray femtosecond transient absorption of vibrational wave packets

Lou Barreau,[1,2,*] Andrew D. Ross,[1,2] Victor Kimberg,[3,†] Pavel Krasnov,[4] Svyatoslav Blinov,[4] Daniel M. Neumark,[1,2,‡] and Stephen R. Leone[1,2,5,§]

[1]*Department of Chemistry, University of California, Berkeley, California 94720, USA*
[2]*Chemical Sciences Division, Lawrence Berkeley National Laboratory, Berkeley, California 94720, USA*
[3]*Department of Theoretical Chemistry and Biology, KTH Royal Institute of Technology, 10691 Stockholm, Sweden*
[4]*International Research Center of Spectroscopy and Quantum Chemistry–IRC SQC, Siberian Federal University, Krasnoyarsk 660041, Russia*
[5]*Department of Physics, University of California, Berkeley, California 94720, USA*

(Received 20 April 2023; accepted 7 June 2023; published 10 July 2023)

A vibrational wavepacket in SF_6 is created by impulsive stimulated Raman scattering with a few-cycle infrared pulse and mapped simultaneously onto five sulfur core-excited states using table-top soft x-ray transient absorption spectroscopy between 170 to 200 eV. The femtosecond vibrations induce real-time energy shifts of the x-ray absorption, whose amplitude depend strongly on the nature of the core-excited state. The pump laser intensity is used to control the number of vibrational states in the superposition, thereby accessing core-excited levels for various extensions of the S-F stretching motion. This enables the determination of the relative core-level potential energy gradients for the symmetric stretching mode, in good agreement with TDDFT calculations. This experiment demonstrates a new means of characterizing core-excited potential energy curves.

DOI: 10.1103/PhysRevA.108.012805

Molecular potential energy surfaces (PESs) dictate the coupled electron-nuclear dynamics following electronic excitation. In particular, PESs of core-excited states are of considerable interest because core-level excitation can induce ultrafast nuclear motion on a timescale shorter than the few-femtosecond core-hole lifetime [1–3]. The x-ray absorption spectrum of a molecule in its vibrational ground state probes only a small region of the PES, at the equilibrium geometry of the ground electronic state. To access a larger range of the core-excited PES, multiple infrared (IR) pump, x-ray probe schemes have been theoretically proposed [4–9]; the IR pulse excites the molecule to higher vibrational states where the nuclear wavepacket has a larger spatial extension, so that subsequent absorption of the x-ray pulse can probe regions of the PES that are otherwise inaccessible. The experimental implementation of these proposals requires few-femtosecond to attosecond x-ray pulses, now available at x-ray free electron laser facilities and from table-top sources based on high-order harmonic generation (HHG) [10]. Indeed, x-ray transient absorption spectroscopy is a sensitive probe of structural dynamics [11]; as the geometry changes, the energy of the electronic transition in the x-ray region is modified. This technique has been successfully used to observe vibrational wavepackets in neutral or cationic molecules, often accompanying strong-field ionization in, e.g., Br_2 [12,13], DBr [14], NO [15], CH_3I [16], CH_3Br [17], and C_2H_4 [18], or single-photon and Raman excitation in I_2 [19] and alkyl iodides [20]. In these cases, the vibrational coherence is typically mapped onto a dissociative core-excited state of predominantly $nd^{-1}\sigma^*$ (for halogen-containing species) or $1s^{-1}\pi^*$ character, which corresponds in the single-particle picture to the excitation of a nonbonding core electron to an antibonding molecular orbital.

In this article, we use a combination of IR and soft x-ray (SXR) few-femtosecond pulses to experimentally map a vibrational wavepacket simultaneously onto five sulfur L-core-excited states of SF_6 in the 170 to 200 eV energy range (Fig. 1). The IR pump pulse produces a coherent superposition of vibrational states in the ground electronic state by impulsive stimulated raman scattering (ISRS) [21,22] and the x-ray absorption energy is probed as a function of the time-delay between the two pulses. The amplitude of the oscillations in energy observed in the transient absorption depends strongly on the core-excited state, in agreement with the nature of the populated molecular orbitals and with time-dependent density functional theory (TDDFT) calculations of the core-excited PESs. The intensity of the short IR pulse is used to control the number of vibrational states in the superposition, enabling the extraction of one-dimensional potential energy gradients along normal modes excited by ISRS [23].

The SF_6 molecule is chosen for its numerous S $2p$ core-excited states accessible to SXR excitation. Two of these, the $2p_{3/2}^{-1}\ a_{1g}$ and $2p_{1/2}^{-1}\ a_{1g}$ states, at 172.27 and 173.44 eV, respectively, lie below their respective $2p$ ionization potentials

*Present address: Institut des Sciences Moléculaires d'Orsay, UMR 8214, CNRS, Université Paris-Saclay, Bâtiment 520, 91405 Orsay Cedex, France; lou.barreau@universite-paris-saclay.fr
†kimberg@kth.se
‡dneumark@berkeley.edu
§srl@berkeley.edu

 ©2023 American Physical Society

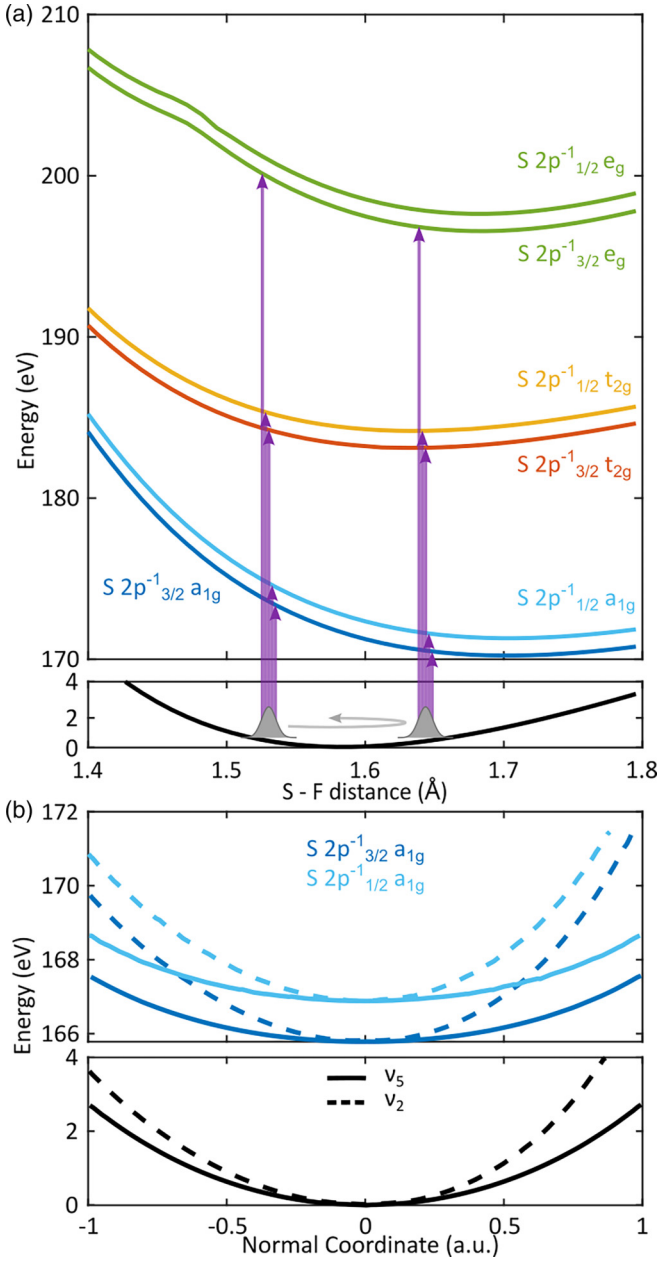

FIG. 1. (a) Illustrative schematic of the experiment principle overlaid on the calculated ground (bottom, black) and core-excited (top) states potential energy curves along the ν_1 mode. (b) Same as (a) along the ν_2 (dashed line) and ν_5 (full line) modes.

at 180.27 and 181.48 eV. In addition, the transitions to the $2p^{-1}_{3/2}\ t_{2g}$, $2p^{-1}_{1/2}\ t_{2g}$ and $2p^{-1}\ e_g$ states lying at 183.40, 184.57, and 196.2 eV, respectively, have been previously assigned to shape resonances as they lie well above the $2p$ ionization thresholds [24,25]. This polyatomic molecule possesses 15 vibrational modes but due to its high symmetry many of them are degenerate. Among those, three are Raman-active [26]: the symmetric stretch ν_1 of A_{1g} symmetry ($\nu_1 = 775$ cm^{-1}, $T_1 = 43$ fs), the antisymmetric stretch ν_2 of E_g symmetry ($\nu_2 = 643$ cm^{-1}, $T_2 = 52$ fs), and the bend ν_5 of T_{2g} symmetry ($\nu_5 = 525$ cm^{-1}, $T_5 = 63$ fs). They can be excited by ISRS with IR pulses shorter than their vibrational period, and the corresponding multimode wavepacket dynamics have been characterized with high-harmonic spectroscopy [27–30]. Figure 1 shows the relevant ground and core-excited potential energy curves calculated by, respectively, DFT [31] and TDDFT [32] methods using the ORCA software [33] with B3LYP functional [34–36], ano-pVTZ basis set [37], RI approximation [38], and quasidegenerated perturbation theory [39] for spin-orbit coupling inclusion. Preliminarily, the geometry and vibrational modes of SF_6 were calculated by DFT under O_h symmetry constrained with the help of the GAMESS software [40] using the B3LYP functional and def2-TZVP basis set [41]. Along the ν_1 mode [Fig. 1(a)], the minima of the $2p^{-1}\ a_{1g}$ and $2p^{-1}\ e_g$ curves appear strongly shifted with respect to the ground state's. On the contrary for the ν_2 and ν_5 vibrational modes [Fig. 1(b)] the core-excited $2p^{-1}\ a_{1g}$ and the ground-state potential energy curves are almost parallel, and there is no displacement of the equilibrium geometry, as expected for nontotally symmetric vibrational modes. The calculated potential energy curves are discussed in relation to our experimental results in the following.

The experimental setup has been described elsewhere [42,43]. Briefly, 85% of the energy of a commercial Ti:sapphire laser delivering 13 mJ, 30 fs, 800 nm pulses is used to pump a multistage optical parametric amplifier that converts the wavelength to 1300 nm. The resulting short-wave infrared (SWIR) pulses are compressed to 12.8 fs full-width at half-maximum (FWHM) with a hollow-core fiber (HCF) compressor, and focused into a semi-infinite gas cell filled with 2 bar of flowing helium for HHG. This yields SXR pulses with a continuous spectrum extending up to 370 eV. The remaining SWIR light is filtered out with a Sn film, and the SXR pulses are focused by a toroidal mirror into a gas cell filled with 25 mbar of SF_6. The SXR spectrum I is measured after dispersion on a grating and imaged onto an x-ray closed coupled device (CCD) camera. The absorbance A is defined as $A = -\log_{10}(I/I_0)$, where I_0 is the spectrum measured without sample.

In the time-resolved experiments, the remaining 2 mJ, 800-nm pulses are compressed in a second HCF compressor to produce 0.75 mJ, 6 fs pulses in the visible-near IR (vis-NIR). After propagation in a piezocontrolled delay line, the vis-NIR pulses are focused with a $f = 37.5$ cm mirror into the gas cell to excite the molecules. The change in absorbance at a delay τ after the pump vis-NIR pulse is $\Delta A(\tau) = -\log_{10}[I_{\text{on}}(\tau)/I_{\text{off}}]$, where I_{on} and I_{off} are the spectra measured with and without the pump pulse at each delay, respectively. The ensemble of pump-off spectra is used for the edge-pixel referencing technique applied to reduce the SXR fluctuations noise in the transient absorption data [44]. In this all-optical experiment, the time and energy resolutions are not interdependent through the uncertainty principle (as opposed to core-level photoelectron spectroscopy that was proposed in Ref. [45] to probe SF_6 vibrations) so that they can be both optimally short and narrow, respectively.

Figure 2(a) shows the absorption spectrum of SF_6 in the vicinity of the S L-edge measured in the absence of the vis-NIR pulse (blue curve). Five peaks are observed, corresponding to the excitation to the spin-orbit split $S\ 2p^{-1}\ a_{1g}$ and $S\ 2p^{-1}\ t_{2g}$ states as well as a broad band attributed to the $S\ 2p^{-1}\ e_g$ doublet, in agreement with reported synchrotron

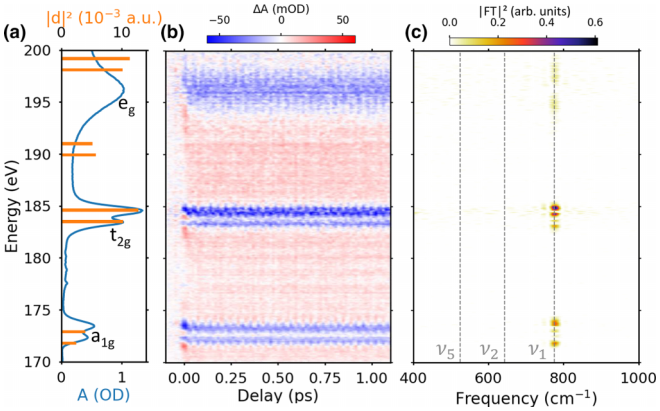

FIG. 2. (a) Measured (blue line) and calculated (orange sticks) SF_6 absorption spectrum at the S $L_{2,3}$ edge. The pre-edge background absorption has been subtracted in the measurement. The calculated energies are shifted by +6.0 eV. The additional doublet of e_g symmetry calculated around 190 eV is not observed in the experiment. (b) Transient absorption spectrogram. Positive delays correspond to the SXR pulse following the vis-NIR pulse. (c) Intensity of the Fourier transform of (b). Frequencies of the ν_1, ν_2, and ν_5 modes are indicated as vertical dashed lines.

data [24]. The orange sticks in Fig. 2 are the results of our B3LYP TDDFT calculations, which agree well with the experimental spectrum for the $S\ 2p^{-1}\ a_{1g}$ and $S\ 2p^{-1}\ t_{2g}$ states. The energy of the $S\ 2p^{-1}\ e_g$ doublet is slightly overestimated around 199 eV, and an additional doublet of e_g symmetry is found around 190 eV. These peaks were previously observed in RT-TDDFT simulations and assigned to t_{2g} symmetry [46], however, their intensity and energy strongly depend on the theoretical approach used [47]. This is probably due to the considerable contribution of shake-up transitions and core-valence double excitations in this resonance [48,49]. The additional doublet is not observed in the experimental spectrum, which suggests that its intensity is overestimated in the theory, and therefore it was excluded from further consideration.

Our discussion focuses now on the dynamics outside of the temporal overlap of the pulses, as opposed to the recent work of Rupprecht *et al.* [50]. The transient absorption of SF_6 after excitation by the $\approx\ 6 \times 10^{14}\,\mathrm{W/cm^2}$ vis-NIR pulse is shown in Fig. 2(b). Clear oscillations of the absorbance are observed at positive delays for the five peaks with a period of $\approx$ 43 fs. The oscillations are long-lived, and the Fourier transform in Fig. 2(c) reveals a single feature at 775 cm^{-1} corresponding to the ν_1 vibrational mode, visible at the energies of all the core-excited levels. With short pump pulses in this intensity range, previous work showed that the three Raman-active modes can be simultaneously excited and probed by high-harmonic spectroscopy [27–30], but only the symmetric stretching motion is observed in our x-ray transient absorption spectroscopy experiment, for reasons detailed later. The positive features appearing at positive delays in-between the assigned peaks in Fig. 2(b) may be attributed to strong-field dissociation of SF_6, although they differ in shape from what was observed in Ref. [51]. Bands attributed to the formation of SF_5^+ in Ref. [51] were not observed under our experimental conditions, despite our higher spectral resolution.

Mapping the same vibrational coherence onto five different core-excited states allows us to compare them. To quantitatively characterize the PES gradients of the five states for the ν_1 normal mode, we use the vis-NIR pump intensity to control the number of vibrational states included in the superposition and therefore the nuclear wavepacket. For ISRS excitation with an electric field $\mathcal{E}$, the nuclear wave function $\chi(q,t)$ satisfies the time-dependent Schrödinger equation (in atomic units)

$$i\frac{\partial\chi(q,t)}{\partial t} = \left(-\frac{1}{2\mu}\frac{\partial^2}{\partial q^2} + V(q) - \frac{1}{2}\sum_{i,j}\alpha_{ij}(q)\mathcal{E}_i(t)\mathcal{E}_j(t)\right) \times\ \chi(q,t), \tag{1}$$

where μ is the reduced mass of the normal mode, V the ground state PES, α the polarizability tensor and $\mathcal{E}_i$ the amplitude of the electric field of the laser pulse along the i axis. For the symmetric stretch mode ν_1 the normal coordinate q identifies with the S-F distance. Figure 3(a) displays the squared nuclear wavepacket $|\chi(q,t)|^2$ in the ground state found from the numerical solution of Eq. (1) with a $6 \times 10^{14}\,\mathrm{W/cm^2}$, 6 fs FWHM Gaussian pump pulse and α and $V(q)$ extracted from DFT B3LYP/def2-TZVP quantum-chemical simulations under constrained O_h symmetry with the GAMESS software. The theoretical PES results in a smaller vibrational frequency than the tabulated value (728 cm^{-1}), giving a slightly longer period of the wavepacket oscillations in Fig. 3(a) compared to the experiment. Figure 4(a) shows the calculated populations of the vibrational levels $\nu_1 = 1$ to 4 after interaction with the pump pulse. At this pump intensity, vibrational levels up to $\nu_1 = 3$ are populated by ISRS. As indicated on Fig. 4(b), the *S-F* distance changes by $\pm$0.092 a.u., which is $\pm$3%, in these conditions.

As the center of the wavepacket oscillates, it is mapped onto the five core-excited PESs. The absorbance measured after excitation with the $6 \times 10^{14}\,\mathrm{W/cm^2}$ vis-NIR pulse with 3 fs delay steps is shown in Figs. 3(b) to 3(d). Apart from a slight difference in frequency originating from the calculated ground-state potential, the absorbance oscillations nicely follow the nuclear wavepacket. No effect of spreading of the wavepacket is observed, indicating excitation of low vibrational levels in the harmonic part of the ground electronic state potential, in agreement with the results of Fig. 4(a). At each delay, the absorption features are fitted by a Gaussian or Lorentzian function depending on the core-excited state [24]. Their central energy oscillates as a function of the vis-NIR–SXR delay with a period of $T_1 = 43$ fs. The oscillations of the central energy are then fitted to a cosine function. Their amplitudes are different for the five core-excited states and inform on their relative PES gradients.

The vis-NIR pump intensity is then varied with a broadband combination of half-waveplate and polarizer between 2.6×10^{14} and $8 \times 10^{14}\,\mathrm{W/cm^2}$. This allows us to incorporate greater or fewer vibrational states in the coherent superposition. As shown on Fig. 5, the calculations indicate that the nuclear wavepacket spatial excursion is linear with the laser intensity in this range, as the maximum vibrational level reached at the highest intensity is $\nu_1 = 4$. A SXR transient absorption spectrogram is measured for six different intensities, all other parameters remaining identical. The amplitude of the

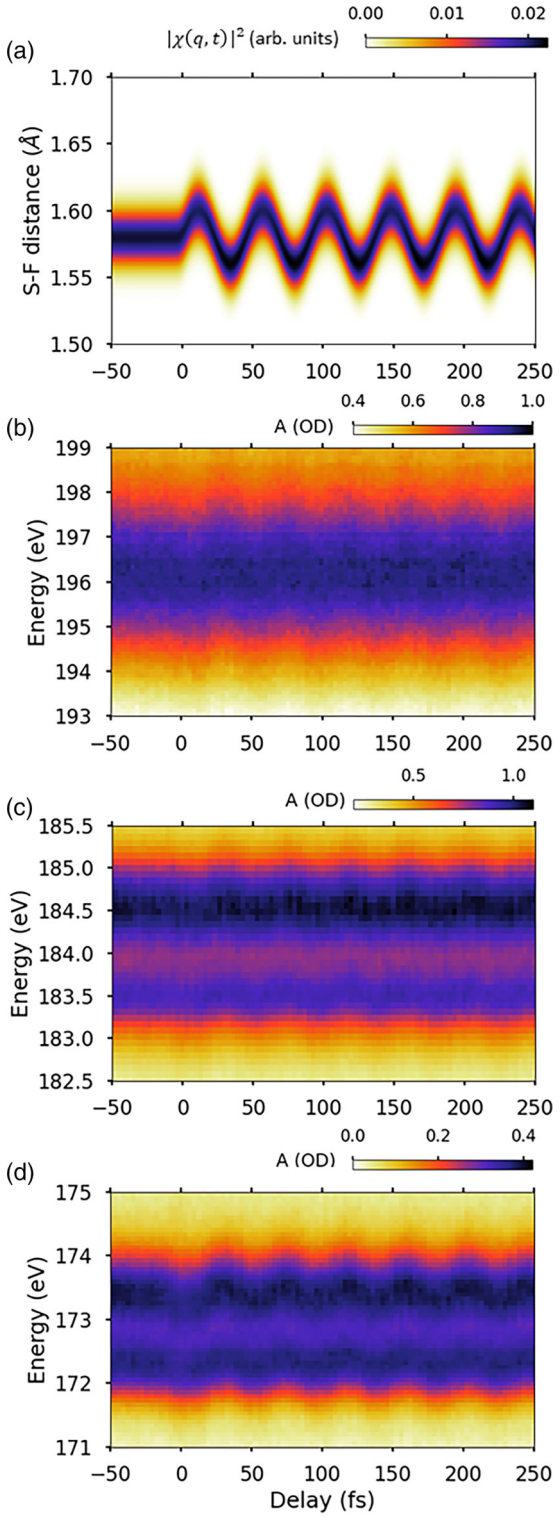

FIG. 3. (a) Simulated nuclear wavepacket after ISRS excitation of the ν_1 mode by a 6 fs, 800 nm pulse of intensity 6×10^{14} W/cm^2. (b)–(d) Measured absorbance $A(\tau)$ for the five core-excited states at the same pump intensity.

central energy oscillation for the five core-excited states at each pump intensity is reported in Fig. 6. For the same nuclear geometry change in the ground state (i.e., at a given pump intensity), the SXR transition energies to the $S\ 2p^{-1}\ a_{1g}$ and

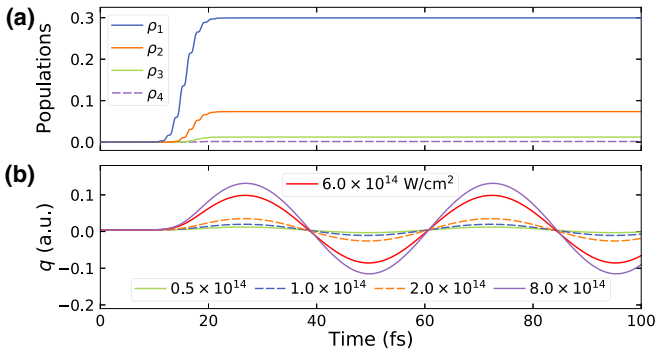

FIG. 4. (a) Calculated populations of the vibrational levels $\nu_1 = 1$ to 4 after interaction with a 6 fs FWHM Gaussian 800 nm pulse of 6×10^{14} W/cm^2 intensity. (b) Calculated average position of the nuclear wavepacket (in atomic units) as a function of time after interaction with a Gaussian 6-fs 800-nm laser pulse of different intensities (indicated in the legend in W/cm^2).

$S\ 2p^{-1}\ e_g$ states have wider excursions from the equilibrium geometry transition compared to the $S\ 2p^{-1}\ t_{2g}$ state. This result reveals the larger displacement of the PES along the S-F bond upon excitation to the $S\ 2p^{-1}\ a_{1g}$ and $S\ 2p^{-1}\ e_g$ states compared to $S\ 2p^{-1}\ t_{2g}$. This different behavior reflects the non-bonding character of the t_{2g} molecular orbital, whereas both the a_{1g} and e_g orbitals are anti-bonding along the S-F bonds (Fig. 6) therefore the electronic energy is more dependent on the internuclear distance.

More quantitatively, the linear increases of the energy shifts with the pump intensity, which gives the spatial extension of the nuclear wave function, can be extracted from a fit of the data in Fig. 6. These shifts are directly related to the gradients of the PESs along the SF distance. With the lowest core-excited state $S\ 2p_{3/2}^{-1}\ a_{1g}$ taken as a reference, the relative PESs gradients are 1.1 ± 0.3 ($S\ 2p_{1/2}^{-1}\ a_{1g}$), 0.45 ± 0.1 ($S\ 2p_{3/2}^{-1}\ t_{2g}$), 0.45 ± 0.1 ($S\ 2p_{1/2}^{-1}\ t_{2g}$), and 1.3 ± 0.4

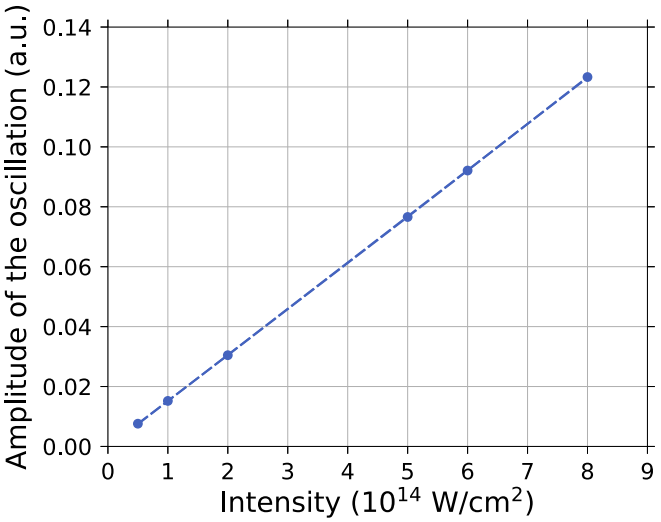

FIG. 5. Amplitude of the calculated oscillation of the average position of the nuclear wavepacket [extracted from Fig. 4(b)] as a function of intensity (dots) and linear fit (dashed line).

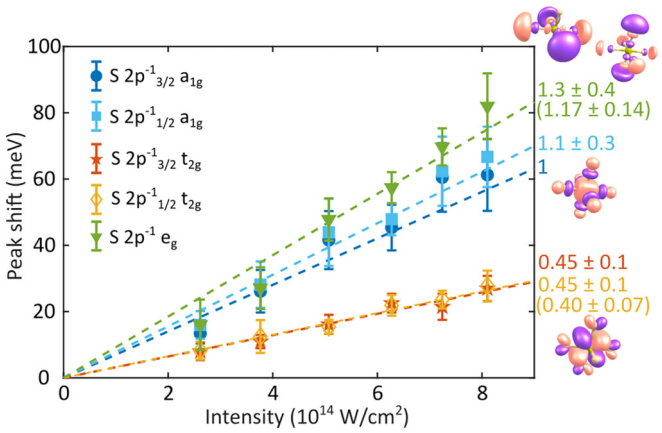

FIG. 6. Amplitude of the absorption peak shift as a function of the pump intensity for the five S core-excited states and their linear fit (dashed line). The error bars represent the 95% confidence bounds. The relative slopes are indicated on the right, with numbers in parenthesis obtained from a fitting procedure including other data sets adapted from [43] and described in the Appendix. Illustrations of the e_g, a_{1g}, and t_{2g} molecular orbitals are shown next to the corresponding state.

($S\ 2p^{-1}\ e_g$) (Fig. 6). The results are consistent with the calculated potential energy curves presented in Fig. 1. As typically observed for core-excited states [3], these PESs have steep gradients along the symmetric stretch mode ν_1, of the order of 10 to 30 eV/Å. At the equilibrium geometry, the gradients of the calculated potential energy curves relative to $S\ 2p^{-1}_{3/2}\ a_{1g}$ are 1.01 ($S\ 2p^{-1}_{1/2}\ a_{1g}$), 0.38 ($S\ 2p^{-1}_{3/2}\ t_{2g}$), 0.38 ($S\ 2p^{-1}_{1/2}\ t_{2g}$), 1.05 ($S\ 2p^{-1}_{3/2}\ 2e_g$), and 1.05 ($S\ 2p^{-1}_{1/2}\ 2e_g$), in good agreement with the experimental values. The e_g doublet is not resolved in practice. The calculated potential energy curves for the ground state and the two lowest core-excited states of a_{1g} symmetry along the normal coordinates of the two other Raman-active modes (ν_2 and ν_5) are shown in Fig. 1(b). The core-excited and ground states are relatively parallel, confirming the lack of observed oscillations in the experiment. A similar behavior is expected for the higher e_g and t_{2g} core-excited states, but vibrations along the non-totally symmetric ν_2 and ν_5 modes lift the degeneracy of these states, making the calculations of the potential energy curves more complex and beyond the scope of this work.

Vibrational dynamics resulting from strong-field ionization have previously been observed with x-ray transient absorption spectroscopy [12–18]. Here, the use of ISRS excitation provides a controlled vibrational wavepacket in the ground electronic state of the molecule. This in turn enables the simultaneous characterization of multiple core-excited potential energy curves. These results are an experimental demonstration of how to probe different regions of the core-excited PESs with the IR pump or x-ray probe scheme theoretically proposed over fifteen years ago [4–6]. Taking advantage of the element specificity of x-ray spectroscopy, multidimensional unexplored regions of core-excited PESs in many systems are accessible with this scheme, implemented either on table-top sources of femtosecond x-ray pulses or free electron lasers. These unexplored regions are expected to drive nuclear dynamics, such as proton transfer in oxygen-core-excited water dimers [6], and could therefore be used to control chemical reactions in short-lived core-excited states.

ACKNOWLEDGMENTS

The authors acknowledge fruitful discussions with Yann Mairesse and Marc Simon. This work is supported by the Gas Phase Chemical Physics program of the U.S. Department of Energy, Office of Science, Office of Basic Energy Sciences, Chemical Sciences, Geosciences and Biosciences Division [Grant No. DE-AC02-05CH11231, FWP No. CH-PHYS01 (D.M.N., S.R.L.)], the National Science Foundation [Grants No. CHE-1951317, No. CHE-2243756, and No. CHE-1660417 (S.R.L.), NSF MRI 1624322 for equipment and A.D.R.], the U.S. Army Research Office under Grant No. W911NF-14-1-0383 (D.M.N., S.R.L.). A.D.R. is also supported by the U.S. Army Research Office Grant No. W011NF-20-1-0127 (D.M.N.) and the W.M. Keck Foundation Grant No. 042982 (S.R.L.). V.K. acknowledges support from the Swedish Research Council (VR) Project No. 2019-03470. P.K. and S.B. acknowledge Russian Foundation for Basic Research (RFBR), Project No. 19-29-12015. L.B. acknowledges support from the Miller Institute for Basic Research in Science at UC Berkeley.

APPENDIX: PHYSICAL PARAMETER EXTRACTION BY LARGE MULTIVARIATE FITTING

The results presented in Fig. 6 were obtained by changing the laser power with a broadband combination of half-wave plate and polarizer, all other parameters (pulse duration, focus size, gas density, etc.) remaining identical. A multivariate fitting procedure to determine the relative potential energy gradients using more experimental datasets (not necessarily measured in exact same conditions) is here presented. To

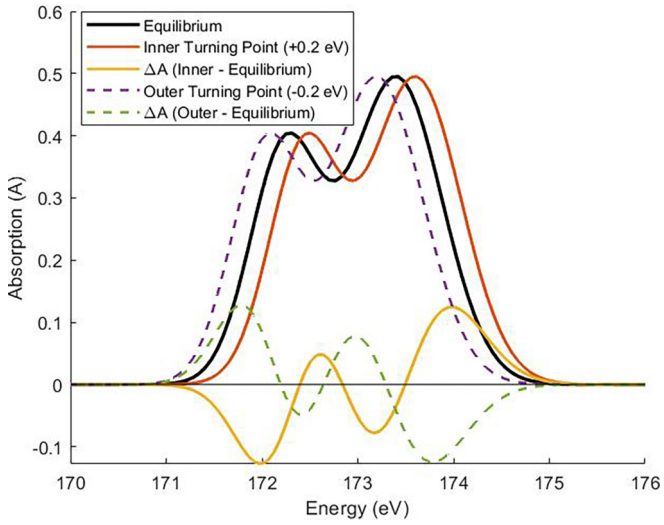

FIG. 7. Illustration of the effect of a ±0.2 eV shift of the peak position on the absorbance and differential absorbance ΔA for peak parameters identical to the $S\ 2p^{-1}\ a_{1g}$ of SF_6. Notice that the ΔA signals are strongest where the slope of the static absorption is the largest.

make use of all of the information provided, the data are fitted to a model that includes vibration and ionization of SF_6.

Due to the nature of measuring vibrations, the transient absorption data has correlations between energy that provide overlapping information. For example, the vibration leads to a net shift of the energy of a state absorption, which leads to a positive ΔA on one side of the energies and a negative ΔA on the other, an example of which is shown in Fig. 7.

After the data for each dataset is prepared, it is saved in files containing the $\Delta A(\tau)$, the static absorption spectrum of SF_6 of that measurement, the delay axis, and the pixel-to-energy calibration axis. A dataset is the set of data taken continuously with no changes to the experiment, usually datasets represent data from different days, but they may also be single days with multiple conditions. Slight differences in energy calibration and sample pressure are determined by comparing the static absorption of each dataset to a master static spectrum. Changes made to internal parameters are made accordingly to energy calibration and pressure to make each dataset comparable to each other. These are all loaded into a single program to fit all of them to a model.

The model is concerned with two different parts: (i) nonoscillatory changes to different electronic states, including ionization, excited states, or extreme nuclear changes, and (ii) oscillatory changes, in this case due to vibration. A complete model of both are necessary for extracting the core-excited potential energy curve (PEC).

(i) The first part of the model follows the general assumption that

$$\Delta A = (P_1 A_1 + P_{\text{neutral}} A_{\text{neutral}}) - A_{\text{static}}$$

where $P_1 + P_{\text{neutral}} = 1$ are coefficients denoting the percent of molecules in a particular state, in this case the ionized SF_6^+ and P_{neutral} is the percent that remains in neutral SF_6 that vibrates. The absorption spectrum A_1 is represented as fitting parameters. These representations only serve to correct for nonoscillatory changes in the ΔA data, which is necessary for extracting the core-excited PEC, but the PEC is the main focus of the fitting. Only delay times greater than 100 fs are used for the fitting procedure to avoid any potential problems that may arise from strong electric field effects or dissociation of SF_6^+.

(ii) The second part of the model is concerned with the oscillatory features due to the vibrations. The main assumption of this part of the model is that the energy of absorption is equal to the energy difference between the PEC of a specific core-excited state and that of the ground state

$$E_{\text{photon}}(q) = \text{PEC}_{\text{core-excited}}(q) - \text{PEC}_{\text{ground}}(q),$$

where q is the movement along the vibrational mode. In the model, $E_{\text{photon}}(q)$ is represented as a polynomial with a potentially variable degree; although, using polynomials that are quadratic or higher degree lead to error bounds too large to make substantive claims. Another assumption is that the vibration occurs in a part of the potential well that harmonic, i.e., that the vibration q position can be denoted by a sine function $q(t) = Q_0 \times \sin[\omega(t - t_0)]$, where Q_0 is the amplitude of vibration, proportional to the pump laser intensity, ω is the frequency of vibration, and t_0 allows for slightly shifted time zeros in each of the individual datasets, relative to time zero. As written in the main text, as no effect of anharmonicity is observed in the experiments at the pump intensities used, this harmonic approximation is valid. The evolution of the absorption with this assumption is simply that the Voigt function of static absorption changes in energy without changing its shape

$$E_{\text{photon}}(t) = E_{\text{polynomial}}\{Q_0 \sin[\omega(t - t_0)]\}.$$

The differential absorbance as a function of time $\Delta A(\tau)$ is then calculated based on this model and is broadened in time by convolution with a Gaussian to account for the temporal

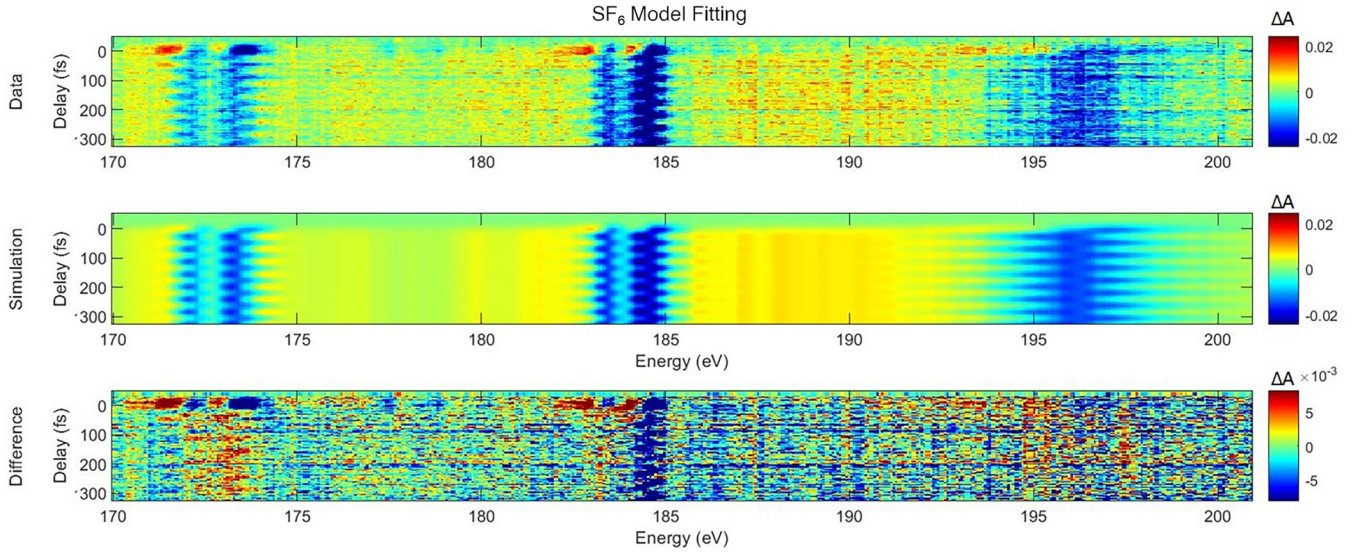

FIG. 8. An example of one dataset fitted by the multivariate fitting algorithm. The top row shows the measured $\Delta A(\tau)$. The middle row shows the result of the fitting. The bottom row shows the difference between the data and the fitting (the top and middle rows). Note that the colorscale on the bottom row is zoomed by a factor of 2.5 to highlight errors. This shows only one dataset. The model ignores the first 100 fs to avoid potential problems arising from dissociation.

resolution of our experiment. The model is subtracted from the data and fed into a minimization of least squares fitting algorithm, LSQNONLIN in MATLAB. The parameters that are needed and common to all datasets are as follows.

(1) Absorbtion spectrum of the new state A_1.
(2) Frequency of the neutral vibration ω.
(3) Core-excited state slopes for the vibration of each transition (polynomial).

The parameters that are unique to each individual dataset are as follows.

(1) Timing delay offset t_0.
(2) Population parameters P_i, for each state in each dataset.
(3) Vibrational amplitude of the neutral Q_0.
(4) Temporal broadening amounts.

An example of a finished fit for one dataset is shown in Fig. 8. Fifteen different datasets are analyzed simultaneously to find the optimal core-excited state PES gradient. The values obtained for the the $S\ 2p^{-1}\ t_{2g}$ and the $S\ 2p^{-1}\ e_g$ are indicated in parentheses on the right side of Fig. 6.

[1] F. Gelmukhanov and H. Ågren, X-ray resonant scattering involving dissociative states, Phys. Rev. A **54**, 379 (1996).

[2] M. Simon, C. Miron, N. Leclercq, P. Morin, K. Ueda, Y. Sato, S. Tanaka, and Y. Kayanuma, Nuclear Motion of Core Excited BF_3 Probed by High Resolution Resonant Auger Spectroscopy, Phys. Rev. Lett. **79**, 3857 (1997).

[3] T. Marchenko, G. Goldsztejn, K. Jänkälä, O. Travnikova, L. Journel, R. Guillemin, N. Sisourat, D. Céolin, M. Žitnik, M. Kavčič, K. Bučar, A. Mihelič, B. C. de Miranda, I. Ismail, A. F. Lago, F. Gel'mukhanov, R. Püttner, M. N. Piancastelli, and M. Simon, Potential Energy Surface Reconstruction and Lifetime Determination of Molecular Double-Core-Hole States in the Hard X-Ray Regime, Phys. Rev. Lett. **119**, 133001 (2017).

[4] V. C. Felicíssimo, F. F. Guimarães, and F. Gel'mukhanov, Enhancement of the recoil effect in X-ray photoelectron spectra of molecules driven by a strong IR field, Phys. Rev. A **72**, 023414 (2005).

[5] F. F. Guimarães, V. Kimberg, V. C. Felicíssimo, F. Gel'mukhanov, A. Cesar, and H. Ågren, Infrared–x-ray pump-probe spectroscopy of the NO molecule, Phys. Rev. A **72**, 012714 (2005).

[6] V. C. Felicissimo, F. F. Guimaraes, F. Gel'mukhanov, A. Cesar, and H. Ågren, The principles of infrared-X-ray pump-probe spectroscopy. Applications on proton transfer in core-ionized water dimers, J. Chem. Phys. **122**, 094319 (2005).

[7] S. Carniato, R. Taïeb, R. Guillemin, L. Journel, M. Simon, and F. Gel'mukhanov, K-L resonant X-ray Raman scattering as a tool for potential energy surface mapping, Chem. Phys. Lett. **439**, 402 (2007).

[8] S. Engin, N. Sisourat, P. Selles, R. Taïeb, and S. Carniato, Probing IR-Raman vibrationally excited molecules with X-ray spectroscopy, Chem. Phys. Lett. **535**, 192 (2012).

[9] N. Ignatova, V. V. da Cruz, R. C. Couto, E. Ertan, M. Odelius, H. Ågren, F. F. Guimarães, A. Zimin, S. P. Polyutov, F. Gel'mukhanov, and V. Kimberg, Infrared-pump–x-ray-probe spectroscopy of vibrationally excited molecules, Phys. Rev. A **95**, 042502 (2017).

[10] L. Young, K. Ueda, M. Gühr, P. H. Bucksbaum, M. Simon, S. Mukamel, N. Rohringer, K. C. Prince, C. Masciovecchio, M. Meyer *et al.*, Roadmap of ultrafast X-ray atomic and molecular physics, J. Phys. B: At. Mol. Opt. Phys. **51**, 032003 (2018).

[11] R. Geneaux, H. J. Marroux, A. Guggenmos, D. M. Neumark, and S. R. Leone, Transient absorption spectroscopy using high harmonic generation: a review of ultrafast X-ray dynamics in molecules and solids, Phil. Trans. R. Soc. A **377**, 20170463 (2019).

[12] E. R. Hosler and S. R. Leone, Characterization of vibrational wave packets by core-level high-harmonic transient absorption spectroscopy, Phys. Rev. A **88**, 023420 (2013).

[13] Y. Kobayashi, K. F. Chang, S. M. Poullain, V. Scutelnic, T. Zeng, D. M. Neumark, and S. R. Leone, Coherent electronic-vibrational dynamics in deuterium bromide probed via attosecond transient-absorption spectroscopy, Phys. Rev. A **101**, 063414 (2020).

[14] Y. Kobayashi, D. M. Neumark, and S. R. Leone, Attosecond XUV probing of vibronic quantum superpositions in Br_2^+, Phys. Rev. A **102**, 051102 (2020).

[15] N. Saito, H. Sannohe, N. Ishii, T. Kanai, N. Kosugi, Y. Wu, A. Chew, S. Han, Z. Chang, and J. Itatani, Real-time observation of electronic, vibrational, and rotational dynamics in nitric oxide with attosecond soft X-ray pulses at 400 eV, Optica **6**, 1542 (2019).

[16] Z. Wei, J. Li, L. Wang, S. T. See, M. H. Jhon, Y. Zhang, F. Shi, M. Yang, and Z.-H. Loh, Elucidating the origins of multimode vibrational coherences of polyatomic molecules induced by intense laser fields, Nat. Commun. **8**, 735 (2017).

[17] H. Timmers, X. Zhu, Z. Li, Y. Kobayashi, M. Sabbar, M. Hollstein, M. Reduzzi, T. J. Martínez, D. M. Neumark, and S. R. Leone, Disentangling conical intersection and coherent molecular dynamics in methyl bromide with attosecond transient absorption spectroscopy, Nat. Commun. **10**, 3133 (2019).

[18] K. S. Zinchenko, F. Ardana-Lamas, I. Seidu, S. P. Neville, J. van der Veen, V. U. Lanfaloni, M. S. Schuurman, and H. J. Wörner, Sub-7-femtosecond conical-intersection dynamics probed at the carbon k-edge, Science **371**, 489 (2021).

[19] S. M. Poullain, Y. Kobayashi, K. F. Chang, and S. R. Leone, Visualizing coherent vibrational motion in the molecular iodine $B\,^3\Pi_{0^+_u}$ state using ultrafast XUV transient-absorption spectroscopy, Phys. Rev. A **104**, 022817 (2021).

[20] K. F. Chang, H. Wang, S. M. Poullain, J. González-Vázquez, L. Bañares, D. Prendergast, D. M. Neumark, and S. R. Leone, Conical intersection and coherent vibrational dynamics in alkyl iodides captured by attosecond transient absorption spectroscopy, J. Chem. Phys. **156**, 114304 (2022).

[21] Y.-X. Yan, E. B. Gamble, Jr., and K. A. Nelson, Impulsive stimulated scattering: General importance in femtosecond laser pulse interactions with matter, and spectroscopic applications, J. Chem. Phys. **83**, 5391 (1985).

[22] Y.-X. Yan and K. A. Nelson, Impulsive stimulated light scattering. I. General theory, J. Chem. Phys. **87**, 6240 (1987).

[23] S. Gerber, S.-L. Yang, D. Zhu, H. Soifer, J. Sobota, S. Rebec, J. Lee, T. Jia, B. Moritz, C. Jia *et al.*, Femtosecond

electron-phonon lock-in by photoemission and X-ray free-electron laser, Science **357**, 71 (2017).

[24] E. Hudson, D. A. Shirley, M. Domke, G. Remmers, A. Puschmann, T. Mandel, C. Xue, and G. Kaindl, High-resolution measurements of near-edge resonances in the core-level photoionization spectra of SF_6, Phys. Rev. A **47**, 361 (1993).

[25] M. Stener, P. Bolognesi, M. Coreno, P. O'Keeffe, V. Feyer, G. Fronzoni, P. Decleva, L. Avaldi, and A. Kivimäki, Photoabsorption and S 2p photoionization of the SF_6 molecule: Resonances in the excitation energy range of 200–280 eV, J. Chem. Phys. **134**, 174311 (2011).

[26] H. H. Claassen, G. L. Goodman, J. H. Holloway, and H. Selig, Raman spectra of MoF_6, TcF_6, ReF_6, UF_6, SF_6, SeF_6, and TeF_6 in the vapor state, J. Chem. Phys. **53**, 341 (1970).

[27] N. L. Wagner, A. Wüest, I. P. Christov, T. Popmintchev, X. Zhou, M. M. Murnane, and H. C. Kapteyn, Monitoring molecular dynamics using coherent electrons from high harmonic generation, Proc. Natl. Acad. Sci. **103**, 13279 (2006).

[28] A. Ferré, D. Staedter, F. Burgy, M. Dagan, D. Descamps, N. Dudovich, S. Petit, H. Soifer, V. Blanchet, and Y. Mairesse, High-order harmonic transient grating spectroscopy of SF_6 molecular vibrations, J. Phys. B: At., Mol. Opt. Phys. **47**, 124023 (2014).

[29] A. Ferré, A. Boguslavskiy, M. Dagan, V. Blanchet, B. Bruner, F. Burgy, A. Camper, D. Descamps, B. Fabre, N. Fedorov *et al.*, Multi-channel electronic and vibrational dynamics in polyatomic resonant high-order harmonic generation, Nat. Commun. **6**, 5952 (2015).

[30] D. Baykusheva, M. S. Ahsan, N. Lin, and H. J. Wörner, Bicircular High-Harmonic Spectroscopy Reveals Dynamical Symmetries of Atoms and Molecules, Phys. Rev. Lett. **116**, 123001 (2016).

[31] P. Hohenberg and W. Kohn, Inhomogeneous electron gas, Phys. Rev. **136**, B864 (1964).

[32] E. Runge and E. K. U. Gross, Density-Functional Theory for Time-Dependent Systems, Phys. Rev. Lett. **52**, 997 (1984).

[33] F. Neese, Software update: the ORCA program system, version 4.0, WIREs Computational Molecular Science **8**, e1327 (2018).

[34] A. D. Becke, Density-functional thermochemistry. III. The role of exact exchange, J. Chem. Phys. **98**, 5648 (1993).

[35] C. Lee, W. Yang, and R. G. Parr, Development of the Colle-Salvetti correlation-energy formula into a functional of the electron density, Phys. Rev. B **37**, 785 (1988).

[36] S. H. Vosko, L. Wilk, and M. Nusair, Accurate spin-dependent electron liquid correlation energies for local spin density calculations: a critical analysis, Can. J. Phys. **58**, 1200 (1980).

[37] F. Neese and E. F. Valeev, Revisiting the atomic natural orbital approach for basis sets: Robust systematic basis sets for explicitly correlated and conventional correlated ab initio methods? J. Chem. Theory Comput. **7**, 33 (2011).

[38] R. Kendall and H. Früchtl, The impact of the resolution of the identity approximate integral method on modern ab initio algorithm development, Theor. Chem. Acta. **97**, 158 (1997).

[39] B. de Souza, G. Farias, F. Neese, and R. Izsák, Predicting phosphorescence rates of light organic molecules using time-dependent density functional theory and the path integral approach to dynamics, J. Chem. Theory Comput. **15**, 1896 (2019).

[40] M. W. Schmidt, K. K. Baldridge, J. A. Boatz, S. T. Elbert, M. S. Gordon, J. H. Jensen, S. Koseki, N. Matsunaga, K. A. Nguyen, S. Su, T. L. Windus, M. Dupuis, and J. A. Montgomery Jr, General atomic and molecular electronic structure system, J. Comput. Chem. **14**, 1347 (1993).

[41] F. Weigend and R. Ahlrichs, Balanced basis sets of split valence, triple zeta valence and quadruple zeta valence quality for H to Rn: Design and assessment of accuracy, Phys. Chem. Chem. Phys. **7**, 3297 (2005).

[42] L. Barreau, A. D. Ross, S. Garg, P. M. Kraus, D. M. Neumark, and S. R. Leone, Efficient table-top dual-wavelength beamline for ultrafast transient absorption spectroscopy in the soft X-ray region, Sci. Rep. **10**, 5773 (2020).

[43] A. D. Ross, D. Hait, V. Scutelnic, E. A. Haugen, E. Ridente, M. B. Balkew, D. M. Neumark, M. Head-Gordon, and S. R. Leone, Jahn-Teller distortion and dissociation of CCl_4^+ by transient X-ray spectroscopy simultaneously at the carbon K- and chlorine L-edge, Chem. Sci. **13**, 9310 (2022).

[44] R. Géneaux, H.-T. Chang, A. M. Schwartzberg, and H. J. Marroux, Source noise suppression in attosecond transient absorption spectroscopy by edge-pixel referencing, Opt. Express **29**, 951 (2021).

[45] N.-T. Nguyen, R. R. Lucchese, C. D. Lin, and A.-T. Le, Probing and extracting the structure of vibrating SF_6 molecules with inner-shell photoelectrons, Phys. Rev. A **93**, 063419 (2016).

[46] M. Kadek, L. Konecny, B. Gao, M. Repisky, and K. Ruud, X-ray absorption resonances near $L_{2,3}$-edges from real-time propagation of the Dirac-Kohn-Sham density matrix, Phys. Chem. Chem. Phys. **17**, 22566 (2015).

[47] T. Fransson, D. Burdakova, and P. Norman, K- and L-edge x-ray absorption spectrum calculations of closed-shell carbon, silicon, germanium, and sulfur compounds using damped four-component density functional response theory, Phys. Chem. Chem. Phys. **18**, 13591 (2016).

[48] T. Ferrett, D. Lindle, P. Heimann, M. Piancastelli, P. Kobrin, H. Kerkhoff, U. Becker, W. Brewer, and D. Shirley, Shape-resonant and many-electron effects in the S 2*p* photoionization of SF_6, J. Chem. Phys. **89**, 4726 (1988).

[49] A. Kivimäki, M. Coreno, P. Miotti, F. Frassetto, L. Poletto, C. Stråhlman, M. De Simone, and R. Richter, The multielectron character of the S $2p \rightarrow 4e_g$ shape resonance in the SF_6 molecule studied via detection of soft X-ray emission and neutral high-Rydberg fragments, J. Electron Spectrosc. Relat. Phenom. **209**, 26 (2016).

[50] P. Rupprecht, L. Aufleger, S. Heinze, A. Magunia, T. Ding, M. Rebholz, S. Amberg, N. Mollov, F. Henrich, M. W. Haverkort, C. Ott, and T. Pfeifer, Laser Control of Electronic Exchange Interaction within a Molecule, Phys. Rev. Lett. **128**, 153001 (2022).

[51] Y. Pertot, C. Schmidt, M. Matthews, A. Chauvet, M. Huppert, V. Svoboda, A. von Conta, A. Tehlar, D. Baykusheva, J.-P. Wolf *et al.*, Time-resolved X-ray absorption spectroscopy with a water window high-harmonic source, Science **355**, 264 (2017).